EPJ Web of Conferences **377**, 02012 (2026) https://doi.org/10.1051/epjconf/202637702012
IPS 2026

Geometric Optimization of Eddy-Current Sensor Coils for Enhanced Sensitivity: A Computational and Experimental Approach

Heri Firmansyah[1*], *Widyaningrum* Indrasari[2], *Wahyu EW* Ndari[2], and *Lutvi Vitria* Kadarwati[3]

[1]Department of Automation Engineering Technology, Universitas Negeri Jakarta, Jakarta 13220, Indonesia
[2]Department of Physics, Universitas Negeri Jakarta, Jakarta 13220, Indonesia
[3]Biomedical Engineering College of Biomedical Engineering, Taipei Medical University, Taiwan

Abstract. Eddy Current Testing (ECT) is a common non-destructive method for detecting flaws in conductive materials such as aluminum and copper, and its detection sensitivity largely depends on the probe coil design. Past studies often lack systematic optimization, leading to suboptimal coils with high resistance and low inductance. This research optimizes transmitter and receiver coils in an ECT system through computational modeling and physical validation to enhance detection capabilities. A Python simulation evaluated key parameters—including the number of turns, coil length, radius, observation distance, and applied current—to compute the resulting magnetic fields and voltages. The computational model was then validated against physical measurements obtained with an LCR meter. The optimal transmitter has 300 turns over 10 layers, with diameters of 6 cm and 7.6 cm, an inductance of 2.59 mH, and a resistance of 1.1 Ω, producing the strongest magnetic field. The receiver uses a 490-turn coil (7.32 mH, 6.4 Ω) to maximize voltage, while a two-coil series reduces resistance to 4.7 Ω and inductance to 2.5 mH for stability. This approach establishes a robust, optimized coil design framework, demonstrating that precise parameter adjustments significantly improve electromagnetic properties and overall signal stability in ECT sensing systems.

1 Introduction

Non-Destructive Testing (NDT) is a technique for testing materials or engineering components without altering their physical condition. NDT encompasses several methods, including Ultrasonic Testing, Radiographic Testing, Magnetic Particle Testing, Eddy Current Testing, Visual Testing, and Penetrant Testing [7]. Eddy Current Testing (ECT) is an electromagnetic NDT method that has been widely developed and used. This method is used across various industrial sectors—such as aerospace, automotive, energy, and manufacturing—to detect surface and subsurface defects in conductive materials [6], thereby

* Corresponding author: heri.firmansyah@unj.ac.id

supporting the goal of SDG 9. The working principle of ECT is based on Faraday's law of electromagnetic induction. When an alternating current (AC) is applied to a transmitter coil, a time-varying magnetic field is generated. This magnetic field induces eddy currents in the surrounding conductive material. The resulting eddy currents produce a secondary magnetic field that interacts with the primary field. This interaction causes an impedance change that can be measured by a receiver coil near the test material [8].

ECT results are influenced by several key factors that determine detection quality, including electrical conductivity, magnetic permeability, operating frequency, lift-off, penetration depth, and skin effect [9-10]. Another crucial factor is the signal-to-noise ratio (SNR), which determines the signal's clarity. The probe coil is the primary component in an ECT system, functioning as both an electromagnetic field inducer and a receiver of signal changes induced by interactions with the test material. The configuration, geometry, number of turns, and coil orientation significantly affect sensitivity, penetration depth, and the system's overall ability to detect defects [1-2].

One of the probe configurations used in ECT systems is the concentric transmitter-receiver (T-R) probe, in which the transmitter and receiver coils are arranged concentrically. In this design, the receiver coil is located at the center and is symmetrically surrounded by the transmitter coil [11]. Optimizing coil design in ECT is essential for enhancing defect-detection sensitivity. Coil shapes and dimensions have been shown to affect the magnetic field distribution and the penetration depth of eddy currents [12].

The performance of an ECT sensor depends heavily on the coil's geometric parameters, such as the number of turns, shape, and effective area. The sensor's sensitivity and linear range depend on the generated magnetic field distribution, with the effective area directly interacting with the conductive target. Experimental results indicate that changes in coil configuration yield significant differences in sensitivity. Furthermore, sensor sensitivity is closely related to variations in mutual inductance between the coil and the test material, which is influenced by the coil's self-inductance. This value depends on the diameter and the number of turns, making the optimization of both factors essential for improving signal quality in ECT systems [3, 13]. Another fundamental consideration in ECT probe design is the receiver coil configuration. Commonly used configurations include absolute (single coil) and differential (multi-coil) types. Previous studies have reported that differential designs can improve sensitivity and penetration depth in detecting buried defects. Conversely, absolute probes are generally used to observe impedance changes caused by material discontinuities. A probe structure featuring dual-excitation coils can generate a broader eddy-current distribution, richer signal information, and higher sensitivity than conventional probes. When multiple excitation coils operate simultaneously, the eddy current fields superpose, thereby increasing signal intensity and expanding the testing area coverage [4, 14].

A relevant previous study developed a conductive plate detection system using a differential concentric-coil probe configuration [15]. The system consisted of one transmitter coil with 350 turns ($L = 2.2$ mH, $R = 1.4\ \Omega$) and two receiver coils, each with 250 turns ($L = 1.66$ mH, $R = 2.7\ \Omega$), connected in series and operating at an excitation frequency range of 10–50 kHz. However, the receiver coils exhibited relatively high resistance ($2.7\ \Omega$), which could limit the signal-to-noise ratio when the induced EMF from the specimen is minimal [5]. Additionally, the receiver coil inductance of 1.66 mH still required optimization to increase the inductive reactance at lower operating frequencies.

This research addresses these limitations by optimizing the geometry of both the transmitter and receiver coils to increase inductance and reduce resistance, thereby theoretically enhancing the ECT system's detection sensitivity to metal objects. Although various studies have examined how geometric parameters affect ECT sensor performance, most remain limited in scope. A Python-based simulation approach—well-suited to resource-constrained research environments—has not been systematically used to compare coil configurations. Specifically, the simultaneous optimization of the number of turns and coil radius still requires a more comprehensive and precise mathematical framework. This paper aims to bridge that gap by developing a Python-based circuit simulation in Google Colab to model the TX-RX coil system over a frequency range of 10 to 100 kHz. Two receiver configurations are compared: a single coil and two coils connected in series. Using computational simulations, this study analyzes the magnetic field distribution and intensity for each configuration to determine the optimal number of turns and coil configuration for maximum sensitivity. The findings are expected to provide practical guidelines for coil design in resource-limited ECT systems.

2 Methodology

2.1 Transmitter and Receiver Coil Simulation

The simulation of the transmitter and receiver coils was conducted in Python within the Google Colab environment, using NumPy for numerical computation and Matplotlib for data visualization. This approach was used to analyze how variations in coil parameters affect the ECT system's performance. Google Colab was selected because it facilitates efficient simulation iteration and visualization of results.

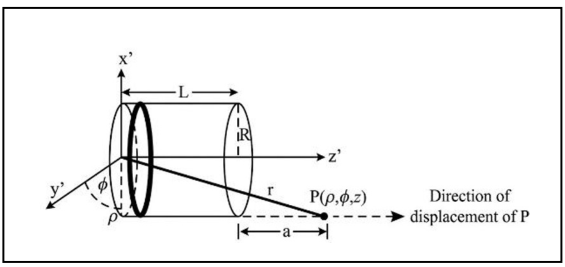

Fig.1. Biot-Savart Law applied to a current-carrying coil.

Based on Figure 1, the Biot-Savart Law, the magnetic field B at an observation point P is determined by the contribution of the current element dI. In this study, point P is located on the central axis of the solenoid, meaning the direction of the current element is perpendicular to the radial distance. By applying boundary conditions to the system, the magnitude of the magnetic field generated by the solenoid can be expressed as follows:

$$B = \frac{\mu_0 NIA}{2\pi R^2}\left[\frac{(L+z)}{(R^2+(L+z)^2)^{1/2}} - \frac{z}{(R^2+z^2)^{1/2}}\right] \mathrm{z} \qquad (1)$$

where μ_0 is the permeability of free space, N is the number of turns in the coil, I is the current (A), A is the cross-sectional area of the coil with radius R, and L is the length of the coil. Furthermore, to determine the magnetic field received by the sensor, sensor 1 is assumed to be located at point P and oriented parallel to the z-axis. Under these conditions, the magnetic field component in the z-direction can be calculated using the equation:

$$B_{z'} = \frac{\mu IA(2z^2-\rho^2)}{4\pi(\rho^2+z^2)^{5/2}}\hat{z} \qquad (2)$$

where the value of ρ is given by:

$$\rho = \sqrt{x^2+y^2} \qquad (3)$$

In this equation (2), $B_{z'}$ is the magnetic field strength in the z'-direction in microteslas (μT), while μ represents the core permeability of the coil. For the purposes of these simulations and subsequent fabrication, the sensors were modeled as air-core coils. Therefore, the core permeability is equal to the permeability of free space ($\mu = \mu_0$). This distinction ensures that the inductance and magnetic field calculations reflect a baseline free of ferromagnetic core saturation effects. The value ρ indicates the projection of the distance from point P to the origin on the $x'y'$-plane, whereas z is the distance between the magnetic field source and the sensor along the z'-axis. This equation is used to calculate the magnetic field contribution due to a single circular wire loop $(n = 1)$ at the observation point $P_1(x_1, y_1, z_1)$. The position of the observation points along the z -direction is expressed as:

$$z_1 = \left(L + a - \frac{nL}{N}\right) \quad (4)$$

where L is the coil length and a is the distance from the end of the coil to point P_1. If the coil consists of N turns, the total magnetic field at the observation point is obtained by summing the magnetic field contributions from each turn, from B_{z1} to B_{zN}.

When the observation points P_1 shifts towards the positive z-axis without changing the values of x_1 and y_1, the value of a and the magnetic field $B_{z'}$ will also change. The computation of the entire magnetic field was performed using Google Colab to determine the most optimal transmitter configuration. The variables were analyzed by inputting the parameters I, N, L, a, and dan R during the optimization process. In this simulation, the permeability of free space μ_0 is set to $4\pi \times 10^{-7}$ H/m to evaluate the magnetic field distribution and determine the coil design that yields the highest sensitivity.

Because the numerical model relies on deterministic analytical equations rather than stochastic processes, standard statistical repetitions are not strictly applicable. Instead, a comprehensive parametric sweep was used, computationally iterating over predefined spatial grids and geometric parameters to identify the configurations that yield the maximum magnetic field intensity.

2.2 Receiver Response Simulation

The receiver simulation was conducted to analyze the receiver coil's response to electromagnetic field changes induced by a metal object. Unlike the transmitter simulation, which focuses on the magnetic field distribution, the receiver simulation emphasizes changes in electrical parameters—such as inductance and output voltage—caused by eddy-current effects. The simulation was carried out using the NumPy library for numerical computation and Matplotlib.

The fundamental principle of the receiver simulation is Faraday's law of electromagnetic induction, which states that the induced electromotive force (EMF) in a coil is proportional to the rate of change of the magnetic flux through it, as shown in Equation 5:

$$\varepsilon = -N\frac{d\Phi}{dt} \quad (5)$$

where script epsilon is the induced EMF, N is the number of coil turns, and Φ represents the magnetic flux. In a transmitter-receiver system, a change in the transmitter coil's current generates a time-varying magnetic field that induces a voltage in the receiver coil. Based on the relationship between the solenoid's magnetic field and the magnetic flux received by the receiver coil, the equation for the induced EMF can be derived as follows:

$$\varepsilon = N_R\,\frac{\mu_0 N_T}{L_T}\,A_R\frac{dI}{dt} \quad (6)$$

where N_R is the number of receiver turns, N_T is the number of transmitter turns, μ_0 is the permeability of free space, L_T is the length of the transmitter coil, A_R is the cross-sectional area of the receiver, and $\frac{dI}{dt}$ is the rate of change of current over time. This equation shows that the induced voltage at the receiver depends on the coil configuration and the variation in the excitation current. When a conductive metal is placed near the system, eddy currents are generated, producing a secondary magnetic field that ultimately affects the magnitude of the induced voltage in the receiver coil.

3 Results and Discussion

3.1 Transmitter Probe Coil Optimization

The initial simulation evaluated the magnetic field (B_z) distribution by varying the number of layers, the total number of turns, and the initial coil diameter to determine the optimal transmitter design.

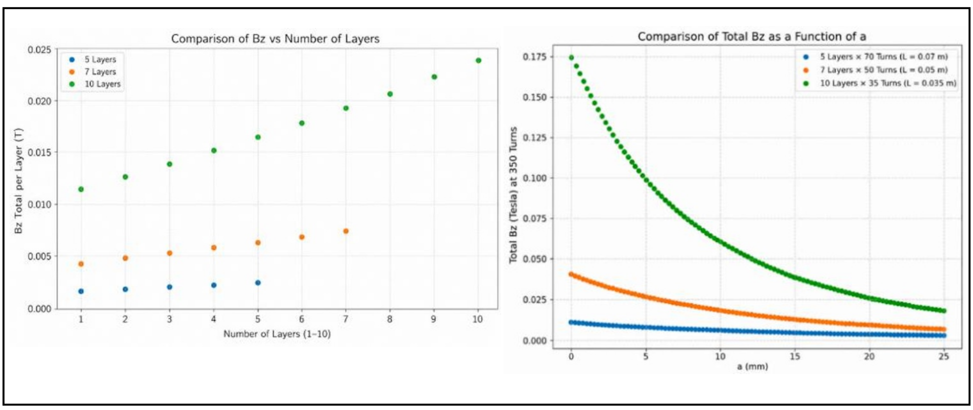

Fig.2. Comparison **graph** of B_z against (a) the number of layers, (b) parameter a.

As shown in Figures 2 (a) and (b), increasing the layer count to 10 significantly amplifies the near-field B_z by creating a more radially structured, centralized turn arrangement that minimizes the effective radial distance (ρ) in accordance with the Biot-Savart law. Although it attenuates rapidly with depth (parameter a), the 10-layer configuration maintains the highest symmetrical peak at the center (x = 0, y = 0), as confirmed by the spatial distribution maps in Figures 3 (a) and (b).

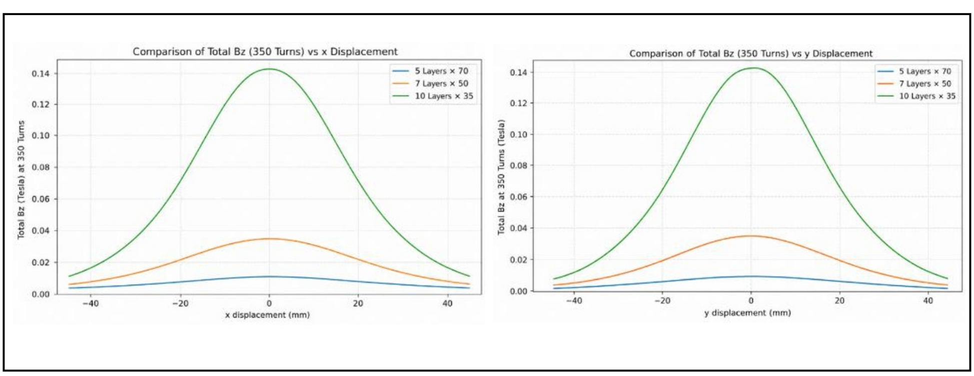

Fig.3. Comparison graph of B_z against (a) x-axis displacement, (b) y-axis displacement.

Subsequent optimization of this 10-layer baseline revealed that increasing the total number of turns counterintuitively reduces the central magnetic field. The second phase of the simulation varied the total number of turns (300, 350, and 400) to assess its effect on the magnetic field. The result demonstrates that the 300-turn configuration outperforms the 350- and 400-turn configurations. Higher turn counts physically widen the overall geometry, displacing the outer turns further from the central axis and diminishing their effective magnetic contribution. Finally, varying the initial coil diameter (Figure 4) established that a 6 cm diameter maximizes the winding area, yielding the highest absolute B_z magnitude and a broader, more evenly distributed magnetic field across the inspection zone.

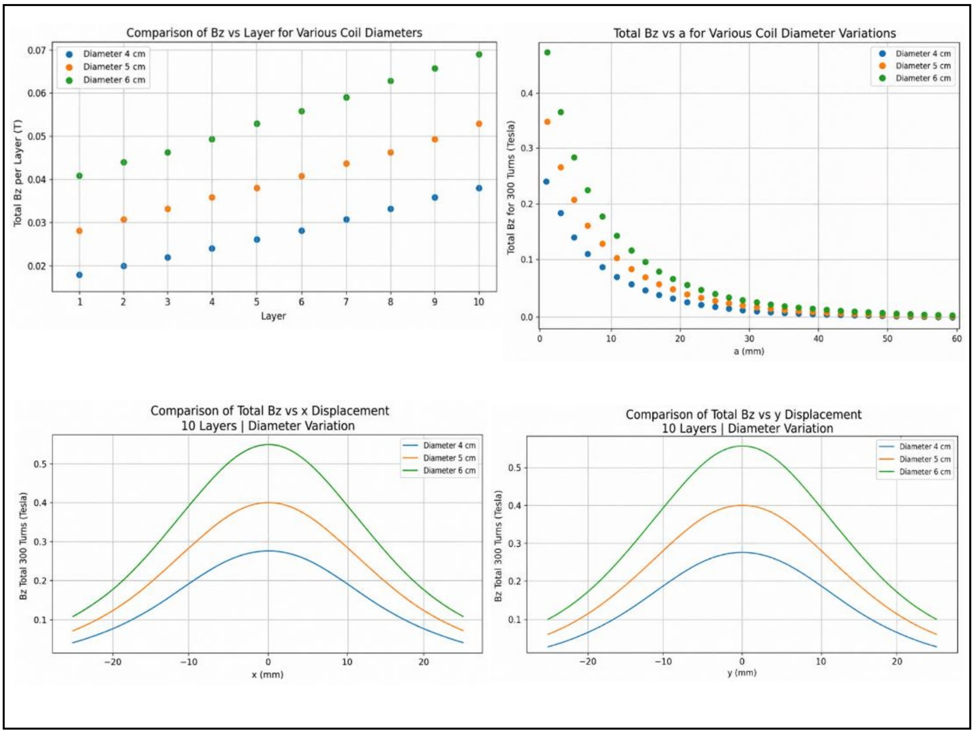

Fig.4. Comparison graph of diameter variation for B_z against (a) the number of layers, (b) parameter a, (c) x-axis displacement, and (d) y-axis displacement.

Consequently, the optimal transmitter probe for resource-limited ECT systems is a 300-turn coil distributed across 10 layers, with an initial diameter of 6 cm, maximizing near-field eddy-current induction.

3.2 Receiver Probe Coil Optimization

The receiver simulation analyzed the induced-voltage response over the 10–100 kHz range. Figure 5(a) shows that the 1-coil (500 turns) and the 2-coil series without a gap (250 + 250 turns) configurations exhibit identical linear increases in induced voltage, driven by the higher rate of change of current $(\frac{dI}{dt})$ according to Faraday's Law. Splitting the coil without introducing a spatial gap maintains optimal magnetic coupling.

However, introducing a gap between the two coils (Figure 5(c)) causes severe magnetic flux leakage, significantly reducing the induced voltage. Furthermore, the receiver coil's inner diameter plays a critical role. As illustrated in Figure 5(b), a 3 cm inner diameter produces a higher induced voltage than a 4.7 cm diameter. The smaller diameter creates a more compact winding space, increasing the effective turn density and maximizing flux linkage.

Despite the simulation indicating that a 3 cm inner diameter maximizes flux linkage and yields optimal induced voltage, the physical prototypes for the receiver coils were constructed with a 4.7 cm inner diameter. This design choice was driven by practical fabrication constraints, specifically the physical dimensions of the available coil bobbins required to mechanically support the 0.5 mm wire gauge and maintain layer stability during winding.

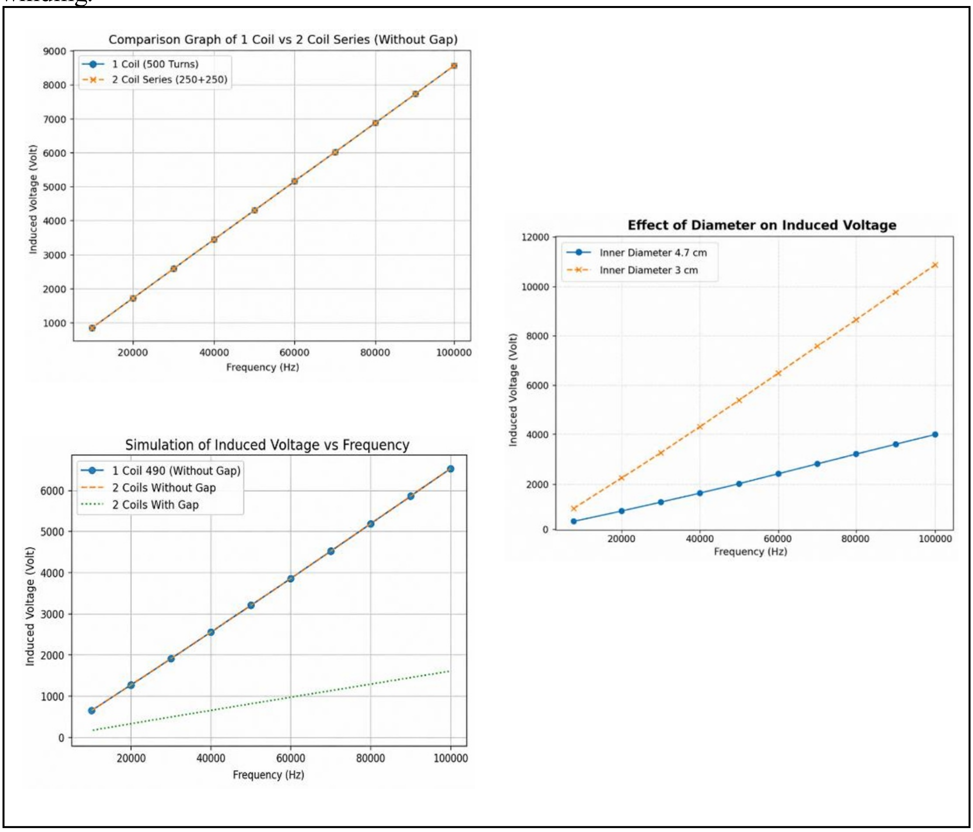

Fig.5. (a) Comparison graph of induced voltage between 1-coil and 2-coil series configurations without a gap against frequency, (b) Graph of the effect of receiver coil inner diameter on induced voltage, (c) Comparison graph of induced voltage for 1-coil, 2-coil series without a gap, and 2-coil series with a gap configuration.

3.3 Prototype Fabrication and LCR Measurements

After the simulation, prototypes of the optimal configurations were fabricated and characterized with an LCR meter (Figure 6). Table 1 lists the physical and electrical parameters of the constructed coils.

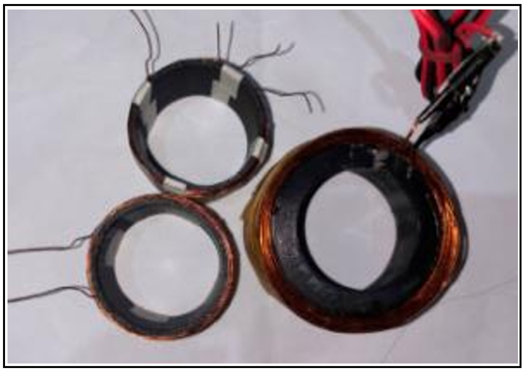

Fig.6. Transmitter and receiver coils.

Table 1. Probe Coil Configuration.

Parameter Coil	Coil Transmitter	Coil Receiver (1 coil)	Coil Receiver (2 coil)
Number of Layers (n)	10	7	7
Number of Turns (N)	300	490	490
Wire Diameter (mm)	1	0.5	0.5
Inner Diameter(cm)	6	4,7	4,7
Outer Diameter (cm)	7,6	5,3	5,2
Coil Height (cm)	4	3,5	3,6
Inductance (mH)	2.59	7.32	2,5
Resistance (Ω)	1.1	6,4	4,7

According to Table 1, the transmitter coil (1.0 mm wire) exhibited a very low resistance of 1.1 Ω and an inductance of 2.59 mH, which is highly advantageous for handling high alternating excitation currents with minimal power dissipation. For the receiver configurations (both using 0.5 mm wire and 490 turns), the single-coil design demonstrated a substantially higher inductance (7.32 mH) than the 2-coil setup (2.5 mH). In ECT applications, this higher inductance theoretically ensures superior sensitivity to minute magnetic flux variations caused by secondary eddy currents. Despite its higher resistance (6.4 Ω), the single-coil receiver's larger inductive reactance at high frequencies compensates for resistive losses, making it the optimal design for capturing weak secondary signals. Compared to prior studies that utilized receiver coils with a high resistance of 2.7 Ω and a lower inductance of 1.66 mH, the optimized single-coil receiver in this study (7.32 mH, 6.4 Ω) demonstrates a significantly higher inductive reactance at operational frequencies. However, it is important to acknowledge certain experimental limitations in this physical validation. The measurements obtained via the LCR meter are subject to inherent measurement uncertainties and potential parasitic capacitance at higher frequencies. Additionally, slight material variability in the copper wire winding can introduce minor deviations between the idealized computational model and the physical prototype.

4 Conclusions

This study establishes a robust framework for optimizing ECT probe coils through precise geometric adjustments that significantly improve electromagnetic performance and signal stability. Computational simulations and physical validations demonstrate that the optimal transmitter configuration consists of 300 turns distributed across 10 layers, with inner and outer diameters of 6 cm and 7.6 cm, respectively. This design produces the strongest, most symmetrically focused magnetic field, achieving an inductance of 2.59 mH and a resistance of 1.1 Ω, while avoiding the reduced central field effectiveness observed in wider geometries. For the receiver, a 490-turn single coil (7.32 mH, 6.4 Ω) maximizes voltage, but a two-coil series configuration reduces resistance to 4.7 Ω and inductance to 2.5 mH. It is critical that this multi-coil arrangement be constructed without a spatial gap to prevent magnetic flux leakage and preserve optimal induced voltage. For complete transparency, several experimental limitations must be acknowledged. While simulations indicated that a smaller inner diameter of 3 cm maximizes the induced voltage due to a more compact winding space, practical bobbin fabrication and manual winding constraints necessitated using a 4.7 cm diameter for the physical prototype. Furthermore, physical measurements are subject to minor experimental uncertainties, variability in copper wire material, and unmodeled parasitic capacitance at higher operational frequencies. Despite these constraints, this systematic parameter optimization significantly enhances defect detection sensitivity, providing highly practical and low-cost design guidelines for industrial applications such as high-speed automated sorting, inline manufacturing inspection, and structural health monitoring. Future research will focus on evaluating the sensor's performance on conductive plates containing actual physical defects, such as fatigue cracks, corrosion, and structural discontinuities, to fully validate its sensitivity in real-world nondestructive testing scenarios.

This publication was funded by the Indonesia Endowment Fund for Education (LPDP) on behalf of the Indonesian Ministry of Higher Education, Science and Technology, and managed under the EQUITY Program (Contract Number 4308/B3/DT.03.08/2025 and B/284/UN39/HK.07.00/2025).

References

1. A. Barrancos, R.L. Batalha, L.S. Rosado, Sensors 23, 2711 (2023). https://doi.org/10.3390/s23052711
2. E. Brun, P.-J. Cottinet, A. Pelletier, et al., Sensors 23, 8345 (2023). https://doi.org/10.3390/s23198345
3. A. Faria, L. Marques, L. Vale, et al., Heliyon 8, e11920 (2022). https://doi.org/10.1016/j.heliyon.2022.e11920
4. J. García-Martín, J. Gómez-Gil, E. Vázquez-Sánchez, Sensors 11, 2525 (2011). https://doi.org/10.3390/s110302525
5. W. Indrasari, et al., J. Phys.: Conf. Ser. 3139, 012047 (2025). https://doi.org/10.1088/1742-6596/3139/1/012047
6. M.A. Machado, Sensors 24, 5819 (2024). https://doi.org/10.3390/s24175819
7. G. Peruń, Materials 17, 554 (2024). https://doi.org/10.3390/ma17030554
8. R. Saddoud, N. Sergeeva-Chollet, M. Darmon, Sensors 23, 4336 (2023). https://doi.org/10.3390/s23094336
9. C. Yan, J. Bao, X. Zheng, Sensors 25, 3900 (2025). https://doi.org/10.3390/s25133900
10. Q. Zhang, X. Li, G. Tian, Stud. Appl. Electromagn. Mech. 45, 27 (2020). https://doi.org/10.3233/SAEM200007
11. R. Zhang, et al., Sensors 22, 6971 (2022). https://doi.org/10.3390/s22186971

12. H.T. Zhou, K. Hou, H.L. Pan, et al., Procedia Eng. 130, 1649 (2015). https://doi.org/10.1016/j.proeng.2015.12.331
13. M.B.G. Sulaiman, J.-Y. Lin, J.-B. Li, et al., Sensors 22, 7854 (2022). https://doi.org/10.3390/s22207854
14. Z. Li, et al., NDT & E Int. 141, 103012 (2024).
15. H.E. Farag, M.B. Khamesee, E. Toyserkani, Sensors 24, 5355 (2024). https://doi.org/10.3390/s24165355